5744 *Macromolecules* **2008**, *41*, 5744−5752

Control of Morphology and Crystallization in Polyelectrolyte/Polymer Blends

Cécile M. Gibon,[†] Sophie Norvez,*,[†] Sylvie Tencé-Girault,[†] and James T. Goldbach[‡]

Matière Molle et Chimie (ESPCI-CNRS, UMR 7167), ESPCI, 10 rue Vauquelin, 75231 Paris Cedex 05, France, and Arkema Inc. Research Center, King of Prussia, Pennsylvania 19406

Received March 19, 2008; Revised Manuscript Received May 30, 2008

ABSTRACT: The type and amount of counterions present in a polyelectrolyte component of a blend with a fluorinated polymer are shown to affect the bulk morphology. Cast films display large-scale phase separation when the polyelectrolyte is in acid form, whereas the blends containing polyelectrolyte fully neutralized with organic counterions are homogeneous. At intermediate ratios, miscibility is controllable, and the blend is partially miscible when cast at 170 °C but fully miscible when cast at 70 °C (LCST behavior). Blend miscibility favors the formation of the β crystalline polymorph of the poly(vinylidene difluoride) component (PVDF). For macrophase-separated systems, the crystalline polymorph depends on the temperature of casting: at 170 °C, the incompatible polymers separate during solvent evaporation and PVDF crystallizes from the melt into the α phase. At 70 °C, PVDF crystallization occurs from a miscible blend during the solvent evaporation and the β phase is obtained, giving rise to crystalline lamellae swollen by the polyelectrolyte.

Introduction

Demixing mechanisms of polymer mixtures in the liquid state are attracting research interest, either for fundamental study of self-organization in nonequilibrium systems of polymers[1−3] or for the more general interest of determining methods to control morphology at various spatial levels, resulting in control of the physical properties of the materials. Polymer blends provide new routes to the design of materials with improved properties compared to those of their constituents. As one example, fuel cell membrane applications have stringent requirements such as high proton conductivity, chemical and mechanical stability, and low water uptake. To design such a material, increasing efforts are being devoted to the development of blended systems.[4,5] Examples include blends of a proton-conductive polymer (typically an ionomer or a polyelectrolyte) with another polymer, chosen to provide good mechanical properties and high stability. PVDF, poly(vinylidene difluoride), which exhibits high chemical and mechanical stability, has already been used for this purpose.[6−10] However, many of these blends display poor mechanical properties and high swelling because macrophase separation occurs between the blend components. Microphase-separated materials such as block copolymers have shown improvements. For example, sulfonated poly(styrene-*b*-ethylene/butylene-*b*-styrene) has been developed,[11,12] whereby a combination of good mechanical properties and high proton conductivity may be optimized. Miscible blends were also obtained by introducing a third copolymer[13] or an organic counterion.[6]

Here, a morphological and microstructural study of a blend of a fluorinated copolymer (PVDF-*co*-hexafluoropropylene (HFP)) with a polyelectrolyte (PAMPS: poly(2-acrylamido-2-methylpropanesulfonic acid)) is presented (Figure 1).

In a previous study, the phase diagram of these immiscible polymers in dimethylformamide (DMF) showed that tetrabutylammonium (TBA$^+$) counterion enhanced the blend miscibility.[14] A low critical solubility temperature (LCST) behavior was also observed in solution. This miscible polymer blend contained one crystallizable component (PVDF), and its solution in good solvent exhibited an unexpected liquid−liquid phase separation at elevated temperature. It thus offered an opportunity to control the bulk morphology as well as its mechanical and transport properties. Here, the morphology and the crystallinity of the materials obtained after solvent evaporation are characterized. The influence of organic counterion and casting temperature on the blend miscibility as well as PVDF crystallization are presented.

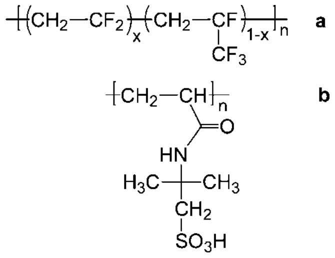

Figure 1. Chemical structure of the polymers: (a) PVDF-*co*-HFP, x = 0.9 wt; (b) PAMPS.

Experimental Section

Materials. The fluorinated copolymer (Arkema Kynar 2801), denoted as PF in this study, is a copolymer of vinylidene difluoride (VDF) and hexafluoropropylene (HFP) (10 wt %) (M_w = 475 000 g/mol, M_w/M_n = 3, T_m = 140−145 °C). Poly(2-acrylamido-2-methyl-1-propanesulfonic acid) (PAMPS) aqueous solution (M_w = 2 × 10^6 g/mol (measured by GPC in aqueous $LiNO_3$ 0.5 M)) and tetrabutylammonium hydroxide (TBAOH) solution in water were purchased from Acros Organics. Anhydrous dimethylformamide (DMF) from Acros Organics was used for the preparation of the solutions. The fluorescent dye $[Ru(bipyridine)_3]Cl_2$ for confocal microscopy was synthesized according to the literature.[15]

Preparation of Neutralized PAMPS. The aqueous PAMPS solutions were freeze-dried, and the resulting powder was further dried under vacuum in the presence of P_2O_5 for 3 days until a controlled amount of bound water equal to 0.5 water per sulfonate group was obtained. The PAMPS neutralization with TBAOH was performed by dilution of a known quantity of PAMPS in water followed by the addition of the desired amount of TBAOH solution. Varying neutralization ratios were prepared by this method (the neutralization ratio is defined as the ratio between the quantity of

---

* Corresponding author. E-mail: sophie.norvez@espci.fr.
[†] ESPCI.
[‡] Arkema Inc. Research Center.

10.1021/ma800612t CCC: $40.75

TBA^+ counterions and the total amount of sulfonate groups). The resulting aqueous solutions were lyophilized, and the powders were stored in a desiccator, where PAMPS hydration did not change with time. A coulometric KF 684 Karl Fischer titrator from Metrohm was used for water titration on 10 wt % polyelectrolyte solutions in DMF.

Preparation of PF/PAMPS Blends. The two polymers were dissolved in DMF in the desired weight fraction of each (total solid concentration of 15 wt %). The molar composition of the blend was kept constant and equal to 85/15 (PF/PAMPS). The corresponding weight composition varied with the neutralization ratio. For neutralization ratios of 0, 25, 50, 75, 100, and 120% with TBA^+, the weight compositions in PF are respectively 65, 59, 54, 50, 46, and 43%. Films (~40 μm thick) were obtained by casting the solutions onto glass plates at varying temperatures. The time necessary for a complete DMF evaporation was dependent on the casting temperature: 80 min at 50 °C, 45 min at 70 °C, 5 min at 170 °C. The films were finally removed from the substrate by immersion in deionized water and dried under ambient atmosphere. No evolution of the film morphology was observed over time.

The film nomenclature is PF-T_c, H-T_c, and *x*TBA-T_c. "PF" refers to the pure PVDF-*co*-HFP films (containing no polyelectrolyte), "T_c" indicates the casting temperature, "H" designates blends containing the acid-form PAMPS, and the "*x*TBA" blends contain a polyelectrolyte neutralized with *x*% of TBA^+ counterions.

Confocal Microscopy. Morphologies were observed using a Zeiss LSM510 inverted microscope equipped with an argon laser (power 30 mW). The films were stained by incorporating a small quantity (<0.02 wt %) of the fluorescent cation $[Ru(bipyridine)_3]Cl_2$ in the DMF solution. The solution was then coated on a cover glass and the solvent evaporated at different temperatures: 50 or 170 °C. These samples were observed directly through the cover glass on which they had been cast. The sample was excited at 458 nm. The collected wavelengths for image formation were selected above 530 nm using a high-band filter. An oil objective with a magnification of 63 and a numerical aperture of 1.4 was used. The corresponding resolutions in the *XY* plane and in the *Z* axis were respectively 130 and 330 nm.

Transmission Electron Microscopy. The blend morphologies were observed using a CEM902 Zeiss transmission electron microscope operating at 80 kV. The films were cut at −80 °C using a ultracryomicrotome (Leica Ultracut UCT). The transverse thin sections of the films (70 nm thickness) were directly transferred from the knife to the C-coated grid and observed without staining.

Swelling Measurements. Films were cut into rectangles of 4 cm (*x*) by 3 cm (*y*) and immersed in 18 MΩ water for 2 h at room temperature. The film size was measured before (x_0, y_0) and after (x_S, y_S) immersion in water, and the swelling was deduced as follows:

$$S_x = \frac{x_S - x_0}{x_0} \times 100$$

$$S_y = \frac{y_S - y_0}{y_0} \times 100$$

The given swelling *S* is the average of the two measurements.

Thermal Analysis. Modulated temperature differential scanning calorimetry (MTDSC) measurements were performed with a TA Instruments Q1000 using a heating rate of 2 °C/min and a temperature modulation of ±0.32 °C every 60 s. Three temperature ramps were applied: first from 20 to 200 °C, second from 200 to −100 °C, and third from −100 to 200 °C. To reduce water evaporation during the first heating ramp, the aluminum pans containing the blend samples were previously dried under vacuum over P_2O_5 for 3 days.

Scattering Techniques. Crystallization was characterized by wide-angle X-ray scattering (WAXS) and small-angle X-ray scattering (SAXS). X-ray scattering experiments were performed at room temperature in transmission mode by using Cu Kα radiation (λ = 1.54 Å) from an X-ray generator (XRG3D Inel) operating at 32 kV and 32 mA. WAXS patterns were collected with a curve position-sensitive detector (CPS120 Inel), and they could be fitted using the Peakoc Inel software for crystallization ratio measurements. SAXS curves were acquired with a linear detector (LPS50 Inel). Two configurations were used to explore a larger range of scattering angles differing only by the sample-to-detector distance, which were chosen at 70.5 and 191.5 cm. The *q* range covered with these two configurations encompassed 0.007−0.18 $Å^{-1}$. SAXS spectra of three films (50TBA-70, 50TBA-170, and 100TBA-170) were also acquired on the ID2 beamline at the European Synchrotron Radiation Facility (ESRF, Grenoble, France), allowing the observation of the scattering intensities at smaller *q* values (from 0.001 to 0.1 $Å^{-1}$). Standard data corrections were applied for both SAXS and WAXS measurements; they have been normalized by the transmission, the thickness, the intensity of the incident beam, the acquisition duration, and finally corrected for background scattering. The scattering profiles were plotted as a function of the scattering vector *q* defined according to eq 1, where Θ is the scattering angle, *d* the Bragg distance, and λ the radiation wavelength.

$$q = \frac{4\pi \sin \Theta}{\lambda} = \frac{2\pi}{d} \qquad (1)$$

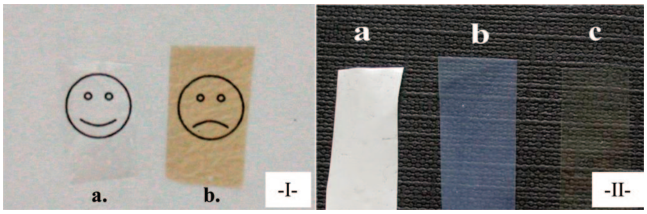

Figure 2. Macroscopic aspect of the films. (I) Influence of the PAMPS hydration state before solvent casting: (a) 0.5 H_2O/SO_3H, (b) 2 H_2O/SO_3H. (II) Influence of the counterion concentration: (a) H-170, (b) 50TBA-170, and (c) 100TBA-170 films.

Results and Discussion

PAMPS was carefully dried and then stored over P_2O_5, and the hydration state was regularly controlled. Under these storage conditions, the polyelectrolyte kept a constant amount of 0.5 water per monomer. In the following, "dry polyelectrolyte" refers to PAMPS containing 0.5 water per monomer. The control of the polyelectrolyte hydration was necessary to precisely control the PAMPS mass for future neutralization or membrane formulation. When stored without any particular care, PAMPS absorbs up to 3 H_2O/SO_3H. In this hydration state, the quantity of polyelectrolyte could be overestimated by 26% if the water content had been neglected. Furthermore, it became apparent that the presence of water within the DMF solution favors PVDF degradation. This degradation is known to occur in the presence of a base to produce conjugated and colored compounds.[16,17] Blends cast in the presence of water were slightly degraded and colored, whereas the blends containing the dry polyelectrolyte were colorless (Figure 2I). Both films correspond to the 120TBA-170 sample; they only differ by the hydration level of the PAMPS used for the formulation.

Morphology Control: Influence of Counterion and Casting Temperature on Blend Miscibility. Films containing PAMPS neutralized with varying amounts of TBA^+ counterions cast at 170 °C present different macroscopic aspects: the H-170 film is white and opaque, the 50TBA-170 blend is translucent, and the 100TBA-170 film is completely transparent (Figure 2II).

Electron micrographs of blends cast into films at 170 and 70 °C are shown in Figure 3. Contrast between phases is provided by the difference in the high electronic density of the semicrystalline PVDF versus amorphous PAMPS (unstained). The H-170 film displays phase separation: PAMPS globules with 500 nm to 1 μm diameter dispersed in a fluorinated matrix (Figure 3a). The 100TBA-170 sample looks completely homo-

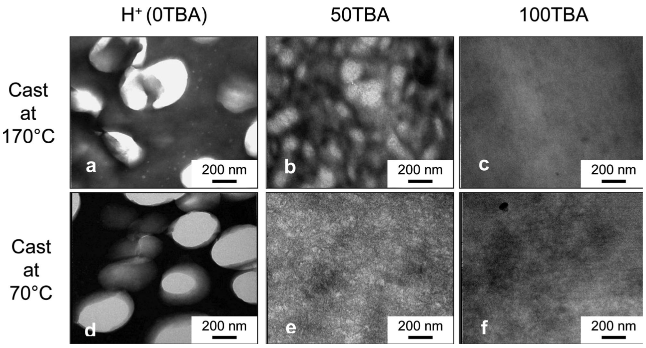

Figure 3. TEM micrographs of PF/PAMPS blends: (a) H-170, (b) 50TBA-170, (c) 100TBA-170, (d) H-70, (e) 50TBA-70, and (f) 100TBA-70 films.

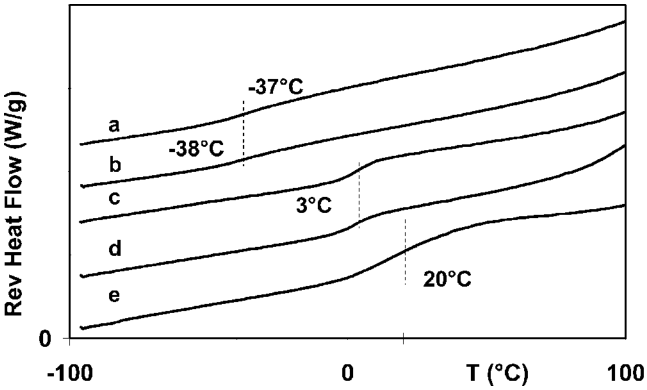

Figure 4. Second heat ramp of TMDSC measurements. Reversing heat flow signal for the (a) Ky-170, (b) H-170, (c) 50TBA-170, (d) 100TBA-170, and (e) 120TBA-170 films.

geneous (Figure 3c). For an intermediate neutralization ratio (Figure 3b), phase separation occurs, but the size of the phase-separated domains is smaller than in the case of the H-170 blend (about 200 nm diameter). In addition, domain borders are diffuse, suggesting the existence of an interphase region corresponding to some interpenetration between phase-separated domains. TEM micrographs thus indicated a gradual miscibility enhancement with increasing TBA^+ neutralization ratios. Such miscibility improvement was already observed in solution.[14]

Modulated temperature DSC (MTDSC) experiments were performed to test the hypothesis of partial miscibility. Despite the preliminary drying step of the pans, a broad peak corresponding to water evaporation appears during the first heating ramp for all samples. Glass transition temperatures of neat PAMPS and blends were thus measured using signals obtained after heating to 200 °C, either during the cooling ramp or during the second heat ramp. The glass transition of the H^+-form PAMPS was measured to be near 100 °C, lower than expected from literature (T_g 175 °C[18]). Glass transitions of the $50TBA^+$- and $100TBA^+$-form PAMPS were found to be 93 and 97 °C, respectively.

The MTDSC traces of the blends cast at 170 °C are presented in Figure 4. The reversing heat flow signal corresponding to the second heat ramp is given. The glass transition temperature for the H-170 and Ky-170 films (−37 °C) corresponds to the PF glass transition; therefore, the blending with H^+-form PAMPS does not interfere with the PF amorphous phase. This result is in agreement with the observation of large-scale phase separation and confirms the incompatibility of PF and PAMPS in H^+-form. The 50TBA-170 and the 100TBA-170 films show similar T_g (3 °C) values, intermediate between the glass transition temperature of PF and the one of the $100TBA^+$-form PAMPS. For the 100TBA-170 film, this glass transition is interpreted as suggestive of blend miscibility also as observed by TEM (Figure 3c). TEM images show that the 50TBA-170 blend displays some phase separation (Figure 3b); however, diffuse interfaces exist suggesting partial miscibility, also supported by an intermediate T_g value. The higher amplitude TMDSC signal measured for the 120TBA-170 film (T_g 20 °C) can be interpreted as a sign of increased amorphous content within the blend.

The MTDSC traces of films cast at 70 and 170 °C are identical (not shown). Differences were noticeable in the TEM images, however. Figure 3d−f shows the morphology of the membranes cast at 70 °C. For intermediate neutralization ratios ($50TBA^+$ systems), macrophase separation occurred for the blend cast at 170 °C (Figure 3b), whereas the images show a higher miscibility in the system cast at lower temperature (Figure 3e) (LCST behavior). The value and amplitude of the glass transition of the 50TBA-70 and 50TBA-170 blends are similar, however. This was expected for the blends containing the H^+-form PAMPS since they all exhibited strict phase separation. For the systems including TBA^+ neutralized polyelectrolyte, the thermal characteristics of samples exhibiting the more or less separated domains were not sufficiently different to be distinguished in DSC. Swelling measurements were performed on the as-cast films, for characterizing the system before the first evaporation. No swelling was observed for the acid-form H-170 and H-70 films. All other samples exhibit a dimensional swelling of about 20%, regardless of the TBA^+ neutralization level and the casting temperature. This swelling behavior confirms at least partial miscibility for all systems in the as-cast form, as the presence of some PAMPS is required to be present within the matrix to achieve such a swelling level.

Confocal microscopy may be used to readily visualize morphological changes by the observation of the fluorescence of a probe introduced into the system. A wide variety of probes are available for confocal microscopy, which can be either simply dissolved within the studied system or attached specifically to the proteins or even to DNA chains.[19] Here, a method to visualize polyelectrolyte demixing is presented. The fluorescent probe used was $[Ru(bipyridine)_3]Cl_2$ complex, a cation able to specifically stain the PAMPS as a counterion. A small amount of this counterion (0.02%), sufficient to display fluorescence, was introduced without disturbing the morphology. Solvent evaporation was performed directly on the cover glass used for microscopic observation, so no supplementary interface was introduced, improving the image resolution. The blends containing the H^+-form PAMPS display large-scale phase separation for all casting temperatures from 170 to 50 °C (fluorescent PAMPS-rich domains dispersed in a dark fluorinated matrix (Figure 5)). The size of the droplets increases with decreasing temperature, which can be rationalized by kinetic effects as the casting time at 170 °C was shorter (5 min (Figure 5a)) than that used at 50 °C (80 min (Figure 5b)); a frozen-in morphology resulted. For all blends with neutralization ratios of 75% or more, no fluorescence contrast was observed. Regardless of casting temperature, all systems displayed homogeneous morphologies at the scale of the observation (75TBA-170 in Figure 5d). Phase-separated domains of PAMPS dispersed in PF were observed for the 50TBA-170 blend (Figure 5c), but at lower casting temperatures, 50TBA-50 and 50TBA-100 show a completely homogeneous morphology. Confocal microscopy thus shows that the miscibility of PAMPS and PF decreases together with decreasing neutralization level (Figure 5a,c) and that a lower casting temperature improves the 50TBA blend miscibility (LCST behavior).

Crystallization Control: Influence of Counterion and Casting Temperature. PVDF crystallizes into polymorphs α, β, γ, and δ.[20–24] The β phase exhibits unique piezo- and

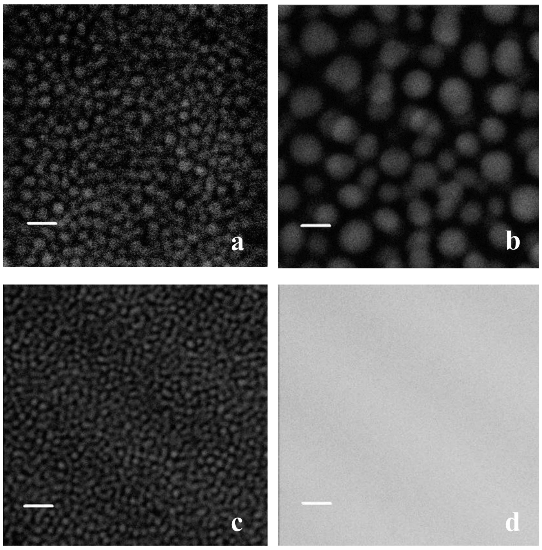

Figure 5. Confocal microscopy images of blends: (a) H-170, (b) H-50, (c) 50TBA-170, and (d) 75TBA-170 blends (scale bar = 2 μm).

pyroelectric properties.[25,26] The processing methodologies giving rise to the different phases in PVDF have been extensively studied.[23] The most common α phase results from melt crystallization at any temperature and predominates for films cast above 110 °C. A mixture of α and β phases is obtained for casting temperatures between 70 and 110 °C, and casting below 70 °C results exclusively in the β phase. Other methods have been developed to produce the β phase, including techniques such as mechanical drawing,[20,27,28] crystallization from specific solvents,[29] crystallization from the melt under high pressure,[30,31] epitaxial growth on a KBr substrate,[32] and poling in high electric fields.[33] Blends with TBA$^+$-form Nafion were proven to crystallize into a mixture of γ and β phases,[6] and the polymorphic composition of PVDF in β phase increases in the blends of PVDF with PMMA.[34]

The effect of casting temperature variation on crystallinity of PF/PAMPS blends is examined here. For blend films cast at 170 °C, the casting temperature is higher than the melting point of PF (145 °C), so that after complete evaporation, the polymer crystallizes from the melt, during rapid cooling to room temperature. Alternatively, by casting at 70 °C, crystallization likely occurs from solution, possibly imparting variation in the nature and amount of crystallinity. Main morphological, thermal, and structural data of these materials are presented in Table 1.

WAXS Experiments. Wide-angle X-ray scattering spectra for the as-cast films (Figure 6) enable the determination of the crystal phases in the different blends as well as the calculation of the crystallization ratio. The spectra of PF-170 and H-170 films are quite similar (Figure 6Ia,b). The characteristic reflections of the α phase are identified in both spectra:[24,35] the indexed Bragg angles (2Θ) are detailed in Table 2. The blending with the H$^+$-form PAMPS does not affect the PF crystallization, and the α phase is obtained. The diffractograms of the blends containing TBA$^+$-PAMPS (50TBA-170, 100TBA-170, and 120TBA-170) are similar (Figure 6IId,e,f); the diffraction angles can be attributed to the β phase. Two of these diffraction peaks observed at $2\Theta = 6°$ and 9.7° are, however, not listed in Table 2 (their corresponding Bragg distances are 14.6 and 9.1 Å, respectively). They are characteristics of the TBA$^+$-form PAMPS, as seen in Figure 6IIg. These diffraction distances would be characteristic of a PAMPS chain conformation, unaffected by blending with PF. Because of a possible presence of the γ phase within the TBA$^+$-containing blends, we compared the different Bragg distances d that could be expected for both phases (γ or β) regarding their structure factor amplitudes.[21,36] Table 2 lists the Bragg distances d that may exhibit the highest diffraction intensities for each phase. The four listed diffraction peaks of the β phase could be easily assigned to the γ phase. Three other intense diffraction peaks from the γ phase are not seen, however. Attempts to fit the diffractograms by introducing these diffraction distances did not give satisfactory results. The observed diffractograms are thus characteristics of pure β crystal polymorph of PF.

The WAXS spectra were all fitted using a Peakoc Inel software which uses pseudo-Voigt profiles. An example of the fit performed for the PF-170 spectrum is presented in Figure 7. The curve fits allow the decomposition of the scattering spectra into amorphous broad peaks (A1 and A2) and crystalline narrow peaks. From this decomposition, the crystallization ratios for each film can be calculated as the ratio between the total intensities of the crystalline peaks and the summed intensities of all peaks. This membrane crystalline ratio is corrected by the composition of the blend to estimate the PF crystallinity. For the PF film, the measured crystallization ratio was 17%. This low crystallinity is due to the presence of the HFP comonomer (pure PVDF crystallinity >20%). The crystallinity of the H-170 film reached 34%. The proportion of crystalline PF within the macrophase-separated blend is double than in the pure PF film, which suggests that the formation of large-scale phase-separated domains might serve as a nucleation agent for the PVDF crystallization. The crystallization ratio of the TBA$^+$-containing blends decreases when the neutralization ratio increases (Table 1).

The crystallite size (L) was estimated using the Scherrer formula[37] given in eq 2, where λ is the Cu Kα radiation wavelength and $\Delta(2\Theta)$ is the peak width at the half-maximum.

$$L = \frac{0.9\lambda}{\Delta(2\Theta)\cos\Theta} \tag{2}$$

The crystallite sizes are similar for pure PF and for the blend with the H$^+$-form PAMPS (around 150 Å). This size is much smaller (below 50 Å) for the blends with the TBA$^+$-PAMPS, showing that the PF crystallization is highly disturbed in miscible blends.

WAXS measurements were performed on blend films cast at lower temperature (70 °C). The diffractogram of the PF-70 film is similar to the one obtained for the film cast at 170 °C (PF-170), in that PF crystallizes into α phase. Various studies have established, however, that crystallization of pure PVDF from a DMF solution at temperatures below 70 °C gives rise to brittle and porous materials crystallized into the β phase.[24,38] Here, the PF-70 film is mechanically flexible and not porous under the same preparation conditions. This difference may be rationalized by the fact that a copolymer containing 10 wt % of hexafluoropropylene was used. The diffractogram of a pure PVDF film, cast in the same conditions as PF-70, showed that PVDF predominantly crystallized into the β phase. The occurrence of α phase for the PF-70 film is thus due to the presence of the HFP comonomer.

The diffractogram of the H-70 blend is presented in Figure 6IIc with the one of the equivalent blends cast at 170 °C (Figure 6Ib). Whereas the H-170 blend crystallized into α phase, the blend cast at 70 °C predominantly crystallized into the β phase. However, as explained earlier, PF-70 shows mainly α phase, which indicates that the presence of the polyelectrolyte favors PVDF crystallization in β phase. The crystallization ratios χ_c measured for the H-70 blend and Ky-70 film are similar (20%, Table 1). The nucleation effect observed for the macrophase-separated blend cast at 170 °C does not occur for the β phase. The TEM images of the H$^+$-form blends show similar morphologies for both casting temperatures with PAMPS domains

Table 1. Morphological and Structural Properties of the PF/PAMPS Films

		MTDSC			WAXS				SAXS
	TEM	T_g (°C)	T_m (°C)	T_c (°C)	phase	A1[a] (Å)	χ_c[b] (%)	L[c] (Å)	L_p[d] (Å)
PF-170	monophasic	−37	146	115	α	4.87	17	150	80
H-170	macroseparated	−38	146	125	α	4.87	34	150	80
50-TBA170	partially miscible	+3	140	107	β	4.52	20	50	80 (broad)
100-TBA170	miscible	+3	134	94	β	4.47	17	50	80 (broad)
PF-70	monophasic				α	4.87	20	150	80
H-70	macroseparated				β	4.65	22	80	80
25-TBA70	partially miscible		same as 170 °C		β	4.56	20	70	130
50-TBA70	miscible				β	4.48	21	50	200
100-TBA70	miscible				β	4.41	14	50	200

[a] A1: position of the first-order amorphous peak. [b] χ_c: PF crystallinity from WAXS spectra decomposition. [c] L: crystallite size estimated from the Scherrer formula. [d] L_p: long period measured from SAXS experiments.

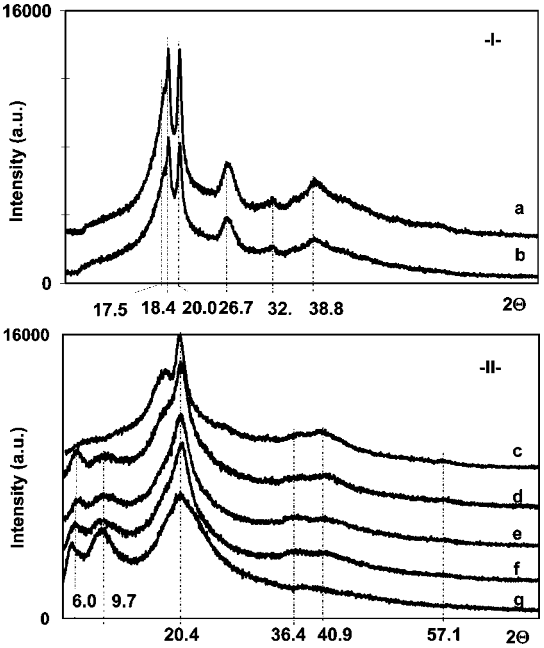

Figure 6. WAXS spectra of the (Ia) PF-170, (Ib) H-170, (IIc) H-70, (IId) 50TBA-170, (IIe) 100TBA-170 (IIf) 120TBA-170 films, and (IIg) PAMPS 100% TBA$^+$.

Table 2. 2Θ and *d* Values of Peaks Observed in Figure 6 and Expected Peak Spacings Associated with the α, β, and γ Phases, after Refs 21, 24, 35, and 36

observed peaks		expected peaks from the literature d (Å)		
2Θ (deg)	d (Å)	α phase	β phase	γ phase
17.5	5.06	5.06		
18.4	4.82	4.83		
19.9	4.46	4.45		4.42
20.4	4.35		4.34	4.3
26.7	3.33	3.34		3.36
32.6	2.74	2.74		
36.4	2.47		2.47	2.48 2.37
38.8	2.32	2.32		
40.9	2.20		2.18	2.14
57.1	1.61		1.61	1.62

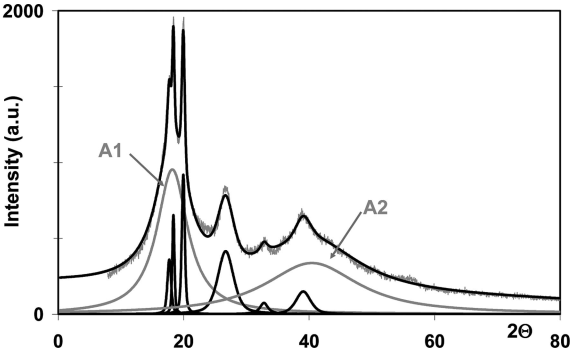

Figure 7. Fit decomposition of the PF-170 spectrum with two broad amorphous peaks (A1, A2 (second order)) and narrow crystalline peaks.

of 500 nm to 1 μm. These two observations indicate that the large-scale phase separation and the crystallization occur simultaneously. TBA$^+$-containing blends cast at 70 °C, crystallized into the β phase as did the equivalent blend cast at 170 °C.

The measured crystallinity ratios decrease as the TBA$^+$ neutralization ratio increases (Table 1). The same crystallite size was found as for the blends cast at 170 °C (50 Å), except for the H-70 blend. The crystallite size of H-70 blend (80 Å) is intermediate between the PF-70 in α phase (150 Å) and the TBA$^+$ blends in β phase (50 Å).

Figure 7 shows that the amorphous phase presents two broad bands. The first order peak (A1) is observed at 4.87 Å, as for all sample crystallized in the α form. The comparison of macroseparated H-170 (α phase) and H-70 (β phase) spectra shows that the peak is shifted toward large angles from α to β (4.65 Å), while for pure acid form PAMPS this amorphous peak was measured at 4.44 Å. The shift is here associated with the nature of the phase, where TBA$^+$-containing blends are crystallized in the β phase, the amorphous peak appearing around 4.5 Å (Table 1). This value is intermediate between the amorphous characteristic distances of PF (β, 4.65 Å) and 100TBA$^+$-PAMPS (4.30 Å) and decreases with the rate of counterion. This continuous change may be associated with the miscibility, at least partial, of the TBA$^+$-containing blends.

Optical Microscopy. Polarized optical micrographs of the as-cast blends are presented in Figure 8. Membranes cast at 170 °C (PF-170, H-170, Figure 8a,b) are both birefringent. The spherulite size for the PF-170 blend is not uniform throughout the thickness of the film, varying from about 10 μm (large and well-defined spherulites) to 2 μm (more coarsely crystallized areas). The shape of the 10 μm spherulites at one side of the film is anisotropic. This anisotropy occurs during the cooling of the film: the substrate influences the crystallization. H-170 film shows smaller spherulites (less than 1 μm), with regular distribution throughout the film thickness. Hence, the presence of the polyelectrolyte and the morphology of the blend influence the crystallization. Birefringence is however still observed, and the crystallization is only slightly disturbed. This is not the case for the TBA$^+$-containing systems: no birefringence is observed. WAXS measurements showed that the crystallinity of TBA$^+$-containing samples was highly disturbed, that the blend film crystallinity ratios were lower than for the PF-170 and H-170 films, and that the crystal polymorph of the TBA$^+$-containing blends is the β phase. The crystallites of the β phase may present

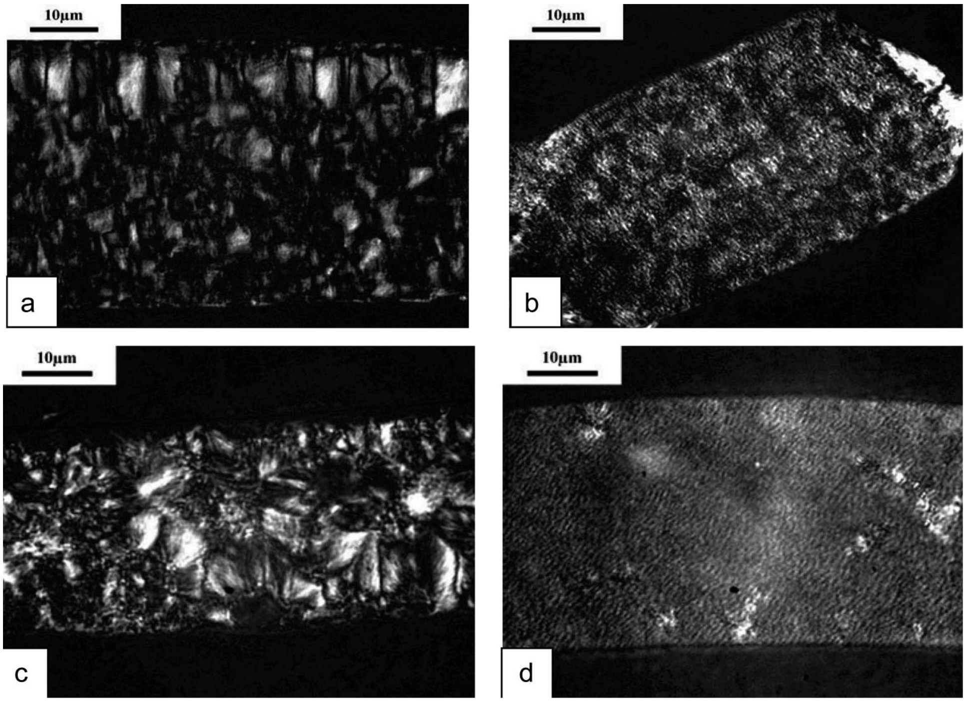

Figure 8. Polarized optical micrographs of the (a) PF-170, (b) H-170, (c) PF-70, and (d) H-70 films.

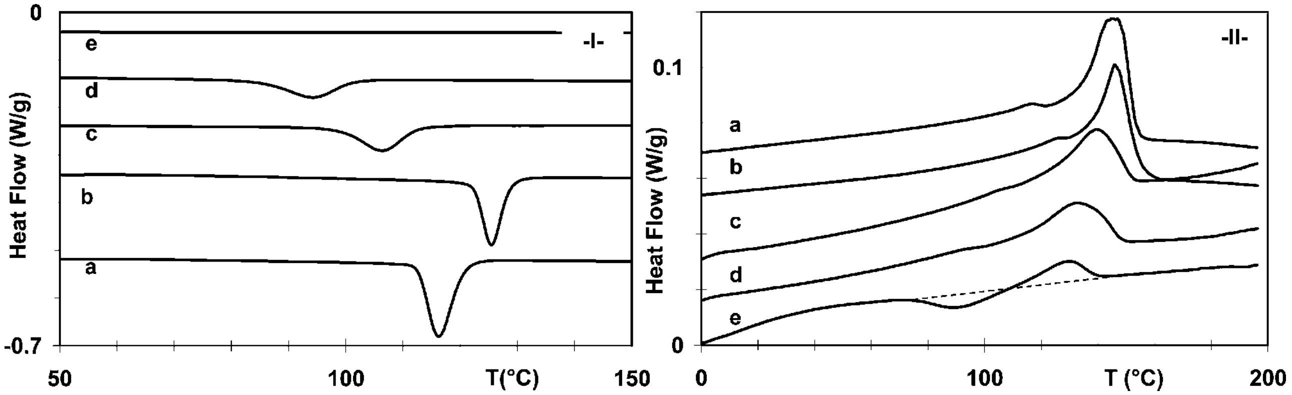

Figure 9. MTDSC measurements (I) cooling ramp and (II) second heating ramp: (a) PF-170, (b) H-170, (c) 50TBA-170, (d) 100TBA-170, and (e) 120TBA-170 films.

less birefringence than those of α phase and thus appear faded. The absence of birefringence within semicrystalline PF samples may then be characteristic of the β phase.

Polarized optical microscopy images of PF-70 and H-70 films cast at lower temperature are shown in Figure 8c,d. Large and well-defined spherulites (10 μm) are observed for the PF-70 film, next to areas displaying smaller crystallized particles. The birefringence observed for the H-70 film is poor compared to that observed for the H-170 blend. This may be associated with the different crystal polymorph of the H-70 blend and confirms that crystallites of the β phase exhibit a dim birefringence. Poorly birefringent and small (<1 μm) crystalline domains are nevertheless still observed, whereas films of TBA$^+$-containing blends are not birefringent at all. The blend miscibility gives rise to a dilution of the crystallinity.

MTDSC Experiments. Cooling ramp and second heating ramp were compared for the different samples (Figure 9). PF crystallization within the different blends is shown in Figure 9I. The crystallization temperature (T_c) of the PF-170 film occurs at 115 °C (Figure 9Ia). For the macrophase-separated blend (H-170 film), the crystallization is observed at a higher temperature (125 °C) (Figure 9Ib, Table 1); thus, the PF crystallization is facilitated within the macrophase-separated blend. This observation is in accordance with the WAXS results indicating a higher crystallization ratio for this blend and with the optical microscopy images showing smaller spherulites, so the macrophase separation would help the nucleation step. On the contrary, the PF crystallization rate is reduced when TBA$^+$ is used as a counterion; therefore, higher neutralization ratios reduce the crystallization temperature (Table 1). PF crystallizes at 107 and 94 °C respectively for the 50TBA-170 and the 100TBA-170 blends, and for the 120TBA-170 film, no crystallization is observed (Figure 9Ie). This crystallization temperature depression is due to the enhanced miscibility of the blend. The PF dilution in PAMPS slows down the transport process of PVDF segments to the crystallite−melt interface that delays the crystallization. This behavior, also observed for other miscible blends with PVDF,[6,39] is considered to be an important factor in the occurrence of the β phase.

Figure 9II shows the second heating ramp for the different blends. Melting of PF-170 and H-170 occurs at the same temperature (146 °C). For TBA$^+$-containing blends, the melting temperature (T_m) decreases with increasing neutralization ratios, as for the first heating ramp. The T_m is observed at 139, 133, and 129 °C for the 50TBA-170, 100TBA-170, and 120TBA-170 films, respectively. This melting point depression could be

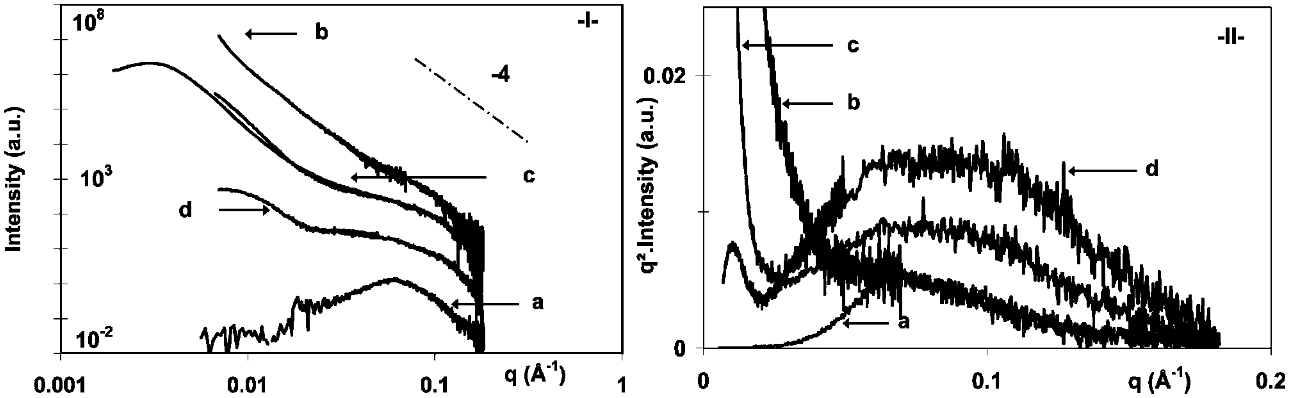

Figure 10. SAXS spectra for the (a) PF-170, (b) H-170, (c) 50TBA-170, and (d) 100TBA-170 films: (I) $I(q)$ plot (for clarity, each profile was shifted vertically) and (II) $q^2I(q)$ plot.

due to morphological causes. However, the favored hypothesis is that the T_m depression is rather a hint of increasing miscibility of PAMPS and PF. First, as mentioned above, the same T_m depression is observed during first or second heating ramps. Second, the miscibility is also supported by the single intermediate T_g of the blend and the depression of the crystallization temperature. Such a behavior was already observed by Nishi and Wang in mixtures of crystalline PVDF and amorphous PMMA[39] and associated with the thermodynamic effect of mixing.

The DSC trace observed for the 120TBA-170 film (Figure 9IIe) shows that the global crystalline ratio is near zero, which is in agreement with the corresponding thermogram of the cooling ramp (no crystallization, Figure 9Ie). Crystallization occurs upon heating; an exothermic peak is observed around 90 °C. Hence, the absence of crystallization during the cooling ramp is only due to kinetic effects.

MTDSC measurements for equivalent blends cast either at 70 or 170 °C show the same behavior. As for T_g determination, MTDSC does not establish differences related to the crystallization process for the blends. The technique however allows the observation of a melting point decreasing for the miscible blends, hint of thermodynamic miscibility, and confirms higher nucleation observed with WAXS for the macrophase-separated blend.

SAXS Experiments. The blend miscibility and crystallinity were further examined by small-angle X-ray scattering (SAXS). The SAXS spectra are given in Figure 10I,II, two different plots of the scattering intensity.

Figure 10I is the log−log plot of the scattering intensity versus the scattering vector (q). The $I(q)$ scattering profile of the PF-170 film (Figure 10Ia) displays a maximum corresponding to the scattering on the interfaces between crystalline and amorphous lamellae. On the log−log representation, this scattering is seen as a q^{-4} regime at large angles (the Porod domain, 0.07 Å^{-1} < q < 0.18 Å^{-1}). The scattering profile of the H-170 blend (Figure 10Ib) is found to be a superposition of two scattering regimes, both displaying a q^{-4} variation. At large q values, the same scattering phenomenon as for pure PF is observed due to the amorphous−crystalline lamellae interfaces. For small q values (q < 0.03 Å^{-1}), the strong scattering is due to the interfaces between phase-separated domains.

The 50TBA-170 and the 100TBA-170 blends display also two scattering phenomena, both displaying a q^{-4} variation. The scattering at large q values is attributed to the amorphous−crystalline interfaces. For the 50TBA-170 blend (Figure 10Ic), the scattering profile measured on the ESRF beamline (superposed to the spectrum obtained with our apparatus) shows diffraction at smaller q values. The second scattering phenomenon observed at small q values (q < 0.018 Å^{-1}) is due to the phase separation. A maximum of the scattering intensity appears for a q value of 0.003 Å^{-1} corresponding to a distance of 200 nm. This distance matches the observed size of the phase separation (Figure 3b). For the 100TBA-170 blend (Figure 10Id), moderate scattering is measured at small q (q < 0.02 Å^{-1}) with a q^{-4} variation. ESRF SAXS measurements confirm that, as in the case of the 50TBA-170 film, a maximum of the scattering intensity is obtained at small q = 0.007 Å^{-1}. Heterogeneities having a characteristic size of 90 nm are thus present within the blend, probably due to the beginning of a phase separation. This phenomenon was not seen in the TEM because of poor electronic contrast associated with the close compositions of the phase-separated domains. SAXS experiments provide here important results on the structuration of the 100TBA-170 blend and demonstrate that phase separation occurs in both blends to a different extent.

The $q^2I(q)$ plots are presented in Figure 10II. The maximum of the $q^2I(q)$ scattering profile corresponds to the long period L_P. From the $q^2I(q)$ representation, the invariant (Inv), corresponding to the integration of the scattering intensity for all q values (eq 3), can be calculated.[40]

$$\mathrm{Inv} = \int_0^\infty q^2 I(q)\, \mathrm{d}q \tag{3}$$

For a two-phase lamellae system, the Invariant can be written[40] as a function of characteristic quantities of the film crystallinity as described in eq 4, where K is a constant determined by the experimental conditions, ρ_C and ρ_A are the electronic densities of the crystalline and the amorphous phases, respectively, and χ_C is the crystallinity ratio of the sample.

$$\mathrm{Inv} = K(\rho_C - \rho_A)^2 \chi_C (1 - \chi_C) \tag{4}$$

From WAXS measurements, the nature of the crystalline phase and the crystallization ratio are known. The only unknown quantities in eq 4 are the experimental constant K and the amorphous electronic density of the blends. The electronic densities of the α and β crystalline polymorphs and of the amorphous phase of PVDF can be calculated from the densities reported in the literature.[41,42] They are found respectively equal to 0.58, 0.59, and 0.51 e$^-$ Å^{-3}. The invariant was calculated for q > 0.02 Å^{-1}.

The long period of PF-170 film was measured at 80 Å (Figure 10IIa). For the pure PF film, ρ_C, ρ_A, and χ_C are known. The calculation of the invariant allows the determination of the experimental constant K, which be used for the calculation of the amorphous densities within the blends. The H-170 spectrum (Figure 10IIb) displays a strong scattering at q < 0.02 Å^{-1} related to large-scale phase separation. An estimation of the two-phase lamellae invariant for this sample can be done after subtraction of the q^{-4} contribution at small angles. The scattering intensity is then characteristic of the PF phase. The crystallinity

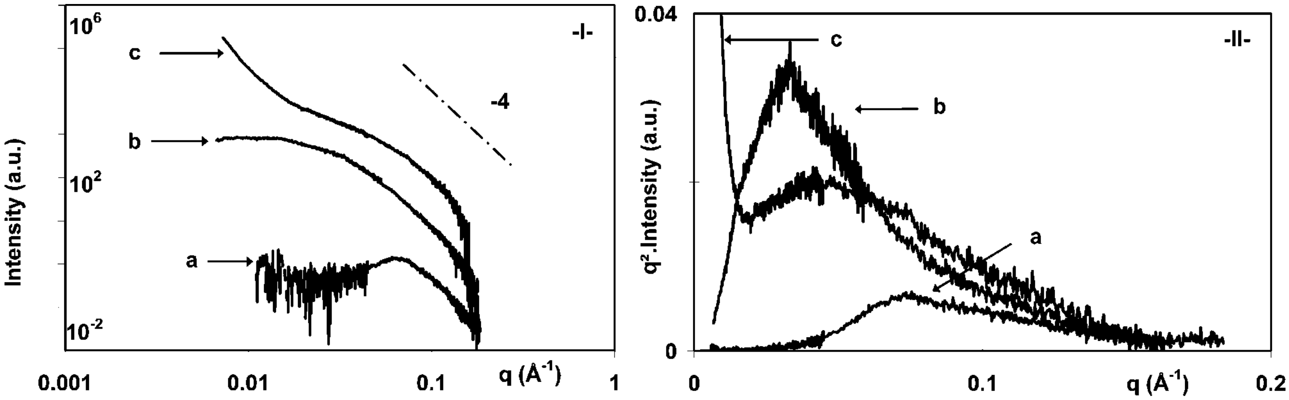

Figure 11. SAXS measurements performed on the (a) PF-70, (b) 100TBA-70, and (c) 25TBA-70 films: (I) $I(q)$ plot (for clarity, each profile was shifted vertically) and (II) $q^2I(q)$ plot.

ratio relevant for the invariant calculation is the one corrected by the membrane composition (Table 1). The amorphous density corresponding to this scattering profile is then supposed to be equal to the one of pure PF. Actually, a densification of the amorphous phase is observed: the electronic density of the amorphous lamellae calculated from the invariant measurement is found equal to 0.54 e^- Å^{-3}. From this, the density of the PF amorphous phase in H-170 is calculated: 1.8 g cm^{-3}. This value corresponds to an increase by 7% of the amorphous density and can be related to the difference in crystallinity ratios between the phase-separated blend (H-170) and pure PF (PF-170). The existence of two different kinds of amorphous phases in PVDF is reported in the literature.[43] These two phases have two different glass transitions: the lower one appearing around −40 °C is attributed to a “free” amorphous phase, whereas the higher one (between 30 and 60 °C) corresponds to an amorphous−crystalline interphase (a−c interphase). The a−c interphase displays higher density than the classical amorphous phase. The proportion of a−c interphase is expected to be higher for high crystallinity samples. This explains the difference of amorphous phase density between PF-170 and H-170, the latter being more crystalline.

The $q^2I(q)$ signal corrected by the q^{-4} contribution at small angles of the H-170 film displays an intensity maximum giving a L_p value around 80 Å: the H-170 and PF-170 films crystallize both into α phase with the same lamellar period. For the 50TBA-170 sample (β phase) (Figure 10IIc), the maximum of the intensity is not as well defined: the system displays a broader distribution for L_p, but this distribution is still centered around 80 Å. Hence, samples cast at 170 °C show the same long period, whatever crystallized into either α or β phases. Indeed, the lamellar period is expected to depend more on the polymer chemistry and thermal history rather than with the nature of the crystal phases.

Besides, scattering intensity for the 50TBA-170 blend is higher than the one measured for the H-170 or PF-170 films. This may be due either to a variation of the membrane crystallinity or to a variation of the amorphous density ρ_A. The calculation of the invariant could not be done for the 50TBA-170 blend, however. Unlike the H-170 membrane, 50TBA-170 displays partial miscibility leading to the formation of two kinds of phase-separated domains with different compositions. These domains consist of an amorphous PAMPS-rich phase and a semicrystalline PVDF rich phase, whose composition is not known. It is thus not possible to estimate the crystallinity of the domains responsible for the large q scattering. Nevertheless, the composition of the amorphous phase is expected to differ from pure PF because of the presence of a certain amount of miscible PAMPS. Then the amorphous density should vary. In addition, the crystalline ratio varies only slightly between pure PF and the 50TBA-170 blend. The higher $q^2I(q)$ intensity may be then related to a decrease of the amorphous density due to the polymer miscibility in the amorphous phase.

The increase of the $q^2I(q)$ intensity is observed to a greater extent for the 100TBA-170 blend (Figure 10IId). Even if the beginning of phase separation is observed at small q, the composition of the blend responsible for the main scattering peak is considered equal to the initial composition of the blend (before phase separation). The relevant crystallinity corresponds then to the membrane crystallinity (before the composition correction). This is a reasonable approximation since the contribution of the peak observed at small q values ($q < 0.02$ Å^{-1}) is found to be negligible in the invariant calculation. The invariant then gives the amorphous electronic density of the blend, 0.39 e^- Å^{-3}. This value is much smaller than the one of pure PF amorphous phase (0.51 e^- Å^{-3}), demonstrating the presence of PAMPS within the amorphous lamella. This quantity can be thus interpreted as a characteristic of the miscible blend composition. As for the 50TBA-170 blend, the PF long period within the 100TBA-170 blend is disturbed: a broader distribution of lamellar sizes (between 60 and 110 Å) is observed. Nevertheless, the mean L_p is still measured around 80 Å.

SAXS spectra of pure PF, 25TBA, and 100TBA blends cast at 70 °C are presented Figure 11. The crystallization of pure PF during solvent evaporation at 70 °C gives the same scattering profile as for the PF crystallized from the melt. The same long period is measured ($L_p = 80$ Å). The scattering profile for the 100TBA-70 blend (Figure 11Ib) is completely different from the one of the 100TBA-170 blend: the $I(q)$ spectrum displays a weak scattering at small q followed by a maximum. In the log−log representation, only one q^{-4} scattering regime is observed over a wide range of q values (0.05 Å^{-1} $< q <$ 0.18 Å^{-1}). This scattering can be attributed to the crystalline−amorphous interfaces. On the $q^2I(q)$ representation (Figure 11IIb), a maximum appears at 0.032 Å^{-1}, indicating a long period of 200 Å. This indicates highly swollen amorphous lamellae compared to the long period measured for the 100TBA-170 blend (80 Å). The spectrum of the 50TBA-70 blend is identical to the one of the 100TBA-70 blend. The same scattering profile was obtained on the ESRF beamline (not shown). SAXS measurements clearly indicate that crystallization occurs during the solvent casting within completely homogeneous blends, incorporating PAMPS in the amorphous phase. MTDSC analyses of 25TBA-70 highlighted the occurrence of an intermediate T_g at 10 °C characteristic of a miscible blend. As for the blends cast at 170 °C, two scattering events with q^{-4} regime are observed for the 25TBA-70 blend, attributed to the phase separation at small q values and to the crystalline organization for larger q values. From the $q^2I(q)$ representation (Figure 11IIc), the long period is determined (130 Å). The swelling is intermediate between the one of PF-70 and the highly swollen lamellae of the 50TBA-70.

According to the invariant, the 100TBA-70 blend displays a lower amorphous density (0.32 e$^-$ Å^{-3}) than the one measured for the equivalent blend cast at higher temperature (0.39 e$^-$ Å^{-3} for the 100TBA-170 blend). Since the 100TBA-170 blend displays some heterogeneity, the amorphous lamella composition may contain a higher amount of PF, increasing the measured density. The crystallization during solvent casting at relatively low temperature may also influence the final density of the blend leading to lower densities by freezing the system before the complete solvent evaporation. The calculation of the electronic amorphous density is though still a characteristic of the blend composition. The lower amorphous density explains at least partly why the long period increases and also confirms that the amorphous blend composition depends on the casting conditions.

SAXS studies of PVDF/PMMA blends[44] have shown that PVDF long period increases strongly with the PMMA content; typically a long period of 200 Å is observed for a PMMA concentration of 40%: the amorphous layers are swelled with PMMA, which is known to be miscible with PVDF. Here, the increase of the long period is observed in the case of completely miscible blends cast at low temperature. The long period for pure PF and for the blends cast at 170 °C is identical, whereas the lamellae are swollen by casting at lower temperature. This is another indication that the miscibility increases at low temperature. This unexpected LCST behavior should be taken into account in the design of homogeneous PVDF/polyelectrolyte membranes for improving transport properties.

Conclusion

The morphology and the crystallization behavior of PF/PAMPS blends have been examined as a function of two parameters: the amount of TBA$^+$ counterion and the casting temperature. TEM observations showed the occurrence of both phase-separated and homogeneous blends. The miscibility at least partial was revealed using swelling measurement and MTDSC. The depression of the PF melting point with increasing ratio of TBA$^+$ counterions indicates the thermodynamic miscibility of the systems involving the TBA$^+$ counterions. SAXS measurements confirmed the miscibility of the TBA$^+$ blends, and a significant amount of PAMPS was found within the amorphous lamellae of the PF. This disturbs the PF crystallization and causes a delay in the crystallization by slowing the transport process of PF segments to the crystallite−melt interface. This could favor the formation of the β crystalline polymorph to the detriment of the α phase within blends exhibiting miscibility. The α phase is only obtained for pure PF and for the macrophase-separated blend.

The casting temperature was also found to highly influence the final blend morphology and crystallinity. TEM observations highlighted a LCST behavior, which was confirmed by SAXS measurements. Even for high neutralization ratios with TBA$^+$, SAXS spectra revealed the presence of heterogeneities within the blends cast at high temperature. Amorphous lamellae were found to be highly swollen by the presence of PAMPS only when cast at low temperature. The present study highlighted the importance of the casting temperature on the mechanism of the film formation; casting at high temperature allowed the system to crystallize only after a complete evaporation of the solvent and during the cooling from the melt to room temperature. On the contrary, by casting below the melting point of PF, the crystallization can occur before the complete solvent evaporation. In this case, the crystallization and phase separation mechanisms compete during the solvent evaporation.

Acknowledgment. The authors acknowledge Arkema for financial support, the LEM laboratory (Arkema Serquigny) for facilitating X-ray scattering experiments, and especially S. Lebreton for her technical help. We are also grateful to E. Di Cola and N. Merlet for sharing their beamline time at the European Synchrotron Radiation Facility (ESRF), Grenoble, to P. Gareil (LECA, ENSCP) for facilitating Karl Fischer measurements, and to Pr. Ludwik Leibler for stimulating discussions and continuous encouragement.

References and Notes

(1) Inaba, N.; Sato, K.; Suzuki, S.; Hashimoto, T. *Macromolecules* **1986**, *19*, 1690–1695.

(2) Svoboda, P.; Keyzlarova, L.; Saha, P.; Rybnikar, F.; Chiba, T.; Inoue, T. *Polymer* **1999**, *40*, 1459–1463.

(3) Olmsted, P. D.; Poon, W. C. K.; McLeish, T. C. B.; Terrill, N. J.; Ryan, A. J. *Phys. Rev. Lett.* **1998**, *81*, 373–376.

(4) Kerres, J. A. *Fuel Cells* **2005**, *5*, 230–247.

(5) Swier, S.; Shaw, M. T.; Weiss, R. A. *J. Membr. Sci.* **2006**, *270*, 22–31.

(6) Landis, F. A.; Moore, R. B. *Macromolecules* **2000**, *33*, 6031–6041.

(7) Ren, S.; Sun, G.; Li, C.; Wu, Z.; Jin, W.; Chen, W.; Xin, Q.; Yang, X. *Mater. Lett.* **2006**, *60*, 44–47.

(8) Cho, K.-Y.; Eom, J.-Y.; Jung, H.-Y.; Choi, N.-S.; Lee, Y. M.; Park, J.-K.; Choi, J.-H.; Park, K.-W.; Sung, Y.-E. *Electrochim. Acta* **2004**, *50*, 583–588.

(9) Mokrini, A.; Huneault, M. A. *J. Power Sources* **2006**, *154*, 51–58.

(10) Chen, N.; Hong, L. *Polymer* **2004**, *45*, 2403–2411.

(11) Weiss, R. A.; Sen, A.; Pottick, L. A.; Willis, C. L. *Polymer* **1991**, *32*, 1867–1874.

(12) Weiss, R. A.; Sen, A.; Pottick, L. A.; Willis, C. L. *Polymer* **1991**, *32*, 2785–2792.

(13) Qiao, J.; Hamaya, T.; Okada, T. *Polymer* **2005**, *46*, 10809–10816.

(14) Gibon, C. M. Fluorinated Polymer/Polyelectrolyte Blend for Fuel Cell Membrane Applications: Structure-Properties Relationship. PhD Thesis, **2006**.

(15) Broomhead, J. A.; Young, C. G. *Inorg. Synth.* **1990**, *28*, 338–340.

(16) Kise, H.; Ogata, H. *J. Polym. Sci., Part A: Polym. Chem.* **1983**, 3443–3451.

(17) Dias, A. J.; McCarthy, T. J. *J. Polym. Sci., Part A: Polym. Chem.* **1985**, *105*, 7–1061.

(18) Travas-Sejdic, J.; Eastal, A. *J. Appl. Polym. Sci.* **2000**, *75*, 619–628.

(19) Brinkley, M. *Bioconjugate Chem.* **1992**, *3*, 2–13.

(20) Lando, J. B.; Olf, H. G.; Peterlin, A. J. *J. Polym. Sci., Part A1* **1966**, *4*, 941–951.

(21) Hasegawa, R.; Takahashi, Y.; Chatani, Y.; Tadokoro, H. *Polym. J.* **1972**, *3*, 600–610.

(22) Doll, W. W.; Lando, J. B. *J. Macromol. Sci., Phys.* **1970**, *4*, 309–329.

(23) Lovinger, A. J. In *Developments in Crystalline Polymers*; Bassett, D. C., Ed.; Applied Science Publishers: London, 1982; Chapter 5.

(24) Gregorio, R., Jr. *J. Appl. Polym. Sci.* **2006**, *100*, 3272–3279.

(25) Bergman, J. G., Jr.; McFee, J. H.; Crane, G. R. *Appl. Phys. Lett.* **1971**, *18*, 203–205.

(26) Nakamura, K.; Wada, Y. *J. Polym. Sci., Part A2* **1971**, *9*, 161–173.

(27) Doll, W. W.; Lando, J. B. *J. Macromol. Sci., Phys.* **1968**, *2*, 205–218.

(28) Matsushige, K.; Nagata, K.; Imada, S.; Takemura, T. *Polymer* **1980**, *21*, 1391–1397.

(29) Miller, R. L.; Raisoni, J. *J. Polym. Sci., Polym. Phys. Ed.* **1976**, *14*, 2325–2326.

(30) Doll, W. W.; Lando, J. B. *J. Macromol. Sci., Phys.* **1970**, *B4*, 889–896.

(31) Scheinbeim, J.; Nakafuku, C.; Newman, B. A.; Pae, K. D. *J. Appl. Phys.* **1979**, *50*, 4399–4405.

(32) Lovinger, A. J. *Polymer* **1981**, *22*, 412–413.

(33) Davis, G. T.; McKinney, J. E.; Broadhurst, M. G.; Roth, S. C. *J. Appl. Phys.* **1978**, *49*, 4998–5002.

(34) Song, D.; Yang, D.; Feng, Z. *J. Mater. Sci.* **1990**, *25*, 57–64.

(35) Bachmann, M. A.; Lando, J. B. *Macromolecules* **1981**, *14*, 40–46.

(36) Weinhold, S.; Litt, M. H.; Lando, J. B. *Macromolecules* **1980**, *13*, 1178–1183.

(37) Klug, H. P.; Alexander, L. E. In *X-ray Diffraction Procedures for Polycrystalline and Amorphous Materials*, 2nd ed.; Wiley-Interscience: New York, 1974.

(38) Young, T.-H.; Huang, J.-H.; Chuang, W.-Y. *Eur. Polym. J.* **2002**, *38*, 63–72.

(39) Nishi, T.; Wang, T. T. *Macromolecules* **1975**, *8*, 909–915.

(40) Glatter, O.; Kratky, O. In *Small Angle X-ray Scattering*; Academic Press Inc.: London, 1982.

(41) *Polymer Handbook*, 4th ed.; Brandrup, J., Immergut, E. H., Grulke E. A., Eds.; Wiley-Interscience: New York, 1999.

(42) Hasegawa, R.; Kobayashi, M.; Tadokoro, H. *Polym. J.* **1972**, *5*, 591–599.

(43) Leonard, C.; Halary, J. L.; Monnerie, L.; Micheron, F. *Polym. Bull.* **1984**, *11*, 195–202.

(44) Ullmann, U.; Wendorff, J. H. *Compos. Sci. Technol.* **1985**, *23*, 97–112.

MA800612T